Mon. Not. R. Astron. Soc. **321**, 723–732 (2001)

A large-eddy simulation of turbulent compressible convection: differential rotation in the solar convection zone

Francis J. Robinson★† and Kwing L. Chan

Department of Mathematics, The Hong Kong University of Science and Technology, Clear Water Bay, Kowloon, Hong Kong, China

Accepted 2000 September 15. Received 2000 September 11; in original form 2000 June 15

ABSTRACT

We present the results of two simulations of the convection zone, obtained by solving the full hydrodynamic equations in a section of a spherical shell. The first simulation has cylindrical rotation contours (parallel to the rotation axis) and a strong meridional circulation, which traverses the entire depth. The second simulation has isorotation contours about mid-way between cylinders and cones, and a weak meridional circulation, concentrated in the uppermost part of the shell.

We show that the solar differential rotation is directly related to a latitudinal entropy gradient, which pervades into the deep layers of the convection zone. We also offer an explanation of the angular velocity shear found at low latitudes near the top. A non-zero correlation between radial and zonal velocity fluctuations produces a significant Reynolds stress in that region. This constitutes a net transport of angular momentum inwards, which causes a slight modification of the overall structure of the differential rotation near the top. In essence, the *thermodynamics controls the dynamics through the Taylor–Proudman momentum balance*. The Reynolds stresses only become significant in the surface layers, where they generate a weak meridional circulation and an angular velocity 'bump'.

Key words: turbulence – Sun: rotation.

1 INTRODUCTION. OBSERVATIONS AND SIMULATIONS

1.1 Observations

In the outer 28 per cent by radius of the Sun, known as the Solar convection zone (SCZ), most of the vertical energy transport is by convection. As a result of the combination of convection and rotation, the gaseous body exhibits differential rotation, i.e. non-uniform angular velocity. Helioseismology observations (Scherrer et al. 1995; Libbrecht 1989) of the nearly 10×10^6 acoustic p-modes that leak from the interior into the atmosphere, have provided through frequency splittings, information on the angular velocity distribution of the solar interior. The latest results suggest that the isorotation surfaces in the solar convection zone are cone-like (aligned radially), in disagreement with most numerical simulations, which tend to produce cylindrical contours parallel to the rotation axis. Specifically, such observations have revealed that: the angular velocity near the equator first increases and then gently decreases with depth, at mid-latitudes it is almost constant with depth, while at high latitudes it increases with depth; on the surface of the Sun, the angular velocity increases from the poles (35-d period) to the equator (25-d period) and the meridional circulation v_θ, is much weaker than differential rotation (zonal velocity $\approx 2\,\mathrm{km\,s^{-1}}$, $v_\theta \approx 25\,\mathrm{m\,s^{-1}}$).

★ E-mail: marjf@astro.yale.edu

† Present address: Astronomy Department, Yale University, Box 208101, New Haven, CT 06520-8101, USA.

1.2 Simulations

1.2.1 Computational hurdles

Modelling the SCZ is a formidable task. Observations suggest that the SCZ is highly stratified, spanning about 19 pressure scaleheights in depth, with the Mach number (the square of the ratio of the flow velocity to the speed of sound) approaching unity at the top; the Prandtl number (the ratio of the time-scales of thermal to viscous diffusion) is extremely small (10^{-6}); the equation of state is complex; and finally, the motion is highly turbulent, as revealed by the large number of scales ranging from 0.1 km to 10^5 km (depth of SCZ). In the photosphere (near the top of the SCZ) the kinematic viscosity of hydrogen is about $0.1\,\mathrm{cm^2\,s^{-1}}$, while the root mean square (rms) velocity in the SCZ is of the order of $100\,\mathrm{m\,s^{-1}}$. These values suggest a Reynolds number, Re = velocity × length/kinematic viscosity, of at least 10^{12}. As the number of degrees of freedom needed to represent a flow is proportional to $\mathrm{Re}^{9/4}$, to resolve numerically the scales in all three directions would require 10^{27} grid points. Even with present technology the maximum Reynolds number modelled in direct numerical simulations (DNS) is a few thousand (Brummel,

Hurlbert & Toomre 1996). Alternatively, if one assumes most of the energy to be contained in the resolved scales, which are much larger than the viscous and thermal dissipation scales (unresolved scales), and that the average energy transferred by these smaller scales can be modelled by entropy diffusion, then a much larger viscosity (smaller Re) can be used to model the turbulent flow. This is the principle of large-eddy simulations (LES).

1.2.2 Numerical simulations of the SCZ

Explicit integration of the hydrodynamic equations requires the time-step to be less than the time for a signal (sound wave) to travel between two grid points. This is known the Courant–Friedrichs–Lévy (CFL) stability criterion. Previous investigations have solved approximate forms of the fully compressible equations, in which sound waves do not exist. This circumvents the use of restrictively small time-steps. Incompressible convection in a shell was studied by Gilman (1978) using the Boussinesq approximation. This allows density variation only when coupled with gravity. A better approximation is to exclude only temporal variations in density, known as the anelastic approximation. This still suppresses sound waves but allows the density to vary vertically. The most recent anelastic simulation in a full shell (global model) on massively parallel architectures are by Miesch et al. (2000). Though there were significant improvements on earlier work (Glatzmaier 1987), they were still unable to adequately resolve the observed cone-like structure of the angular velocity contours. Overall the isorotation contours were cylindrical. Furthermore, the angular velocity shear layer near the top of the convection zone could not be resolved. Near the top, vigorous compressible motions have Mach numbers close to one and the anelastic approximation breaks down.

The fully compressible equations have, however, been solved in local models (boxes). By considering only a tiny section of a spherical shell, Brummel et al. (1996) performed a DNS of turbulent compressible convection in f-planes. In essentially the same geometry, Chan (2001) performed a set of LES computations, in f-planes. The LES model emphasized efficient convection (convective flux $\gg$ diffusive flux) as opposed to the inefficient convection in the DNS models. In f-plane simulations the angle between the rotation vector and gravity is considered to be constant throughout the box. The problem with these local models is that they have periodic horizontal boundaries. In such domains the only possible source of differential rotation is the Reynolds stress. Horizontal averaging removes latitudinal gradients of thermal quantities which are a possible source of the differential rotation. For example, in the model by Durney (1999), the latitudinal entropy gradient (or baroclinicity) is essential in shaping the isorotation contours. Additionally, the f-plane models do not allow a realistic meridional circulation to develop; nor can Rossby waves exist as the rotation vector is constant throughout the domain. Rossby waves have been suggested as a possible source of correlation between longitudinal and meridional motions (Brummel et al. 1996).

Our model represents a compromise between the anelastic global and compressible local simulations. We solve the full Navier–Stokes equations in spherical coordinates in a domain with a significant latitudinal coverage. In this way we are able to resolve the upper shear layers and simultaneously include the effects of meridional circulation and latitudinal gradients of thermal quantities. To circumvent the CFL restriction on the time-step, semi-implicit time integration is employed. We use the alternating direction implicit method on a staggered mesh (ADISM) (Chan & Wolff 1982) in conjunction with an explicit method. Owing to computational restraints of three-dimensional calculations, we are limited to studying a small section of the entire shell. A full simulation on a $70 \times 70 \times 39$ three-dimensional mesh, spans just 60° in longitude and latitude. This calculation requires about a month to run when parallelized on four processors of the ORIGIN 2000.

This paper consists of a further four sections. Section 2 describes the overall physical setup, formulates the mathematical model and describes the numerical approach. This is followed by descriptions of the statistically averaged zonal and meridional flows and the turbulent nature of the compressible convection. Section 3 attempts to pin down the source of the differential rotation and meridional circulation. The final section is a conclusion.

2 MATHEMATICAL MODEL

2.1 Overall setup

The computational domain is a three-dimensional sector of a spherical shell, symmetric about the equatorial plane. A longitudinal cross-section is shown in Fig. 1. The input energy flux at the bottom (straight arrows), is transported mostly by convective eddies (curly arrows) up to a height of 95 per cent of the total depth. To pad out convective motions, a conduction layer is placed in the upper 5 per cent of the shell (shaded region). We consider two models that are identical apart from their longitudinal spans. The first model, denoted A, spans 30° in longitude and 60° in

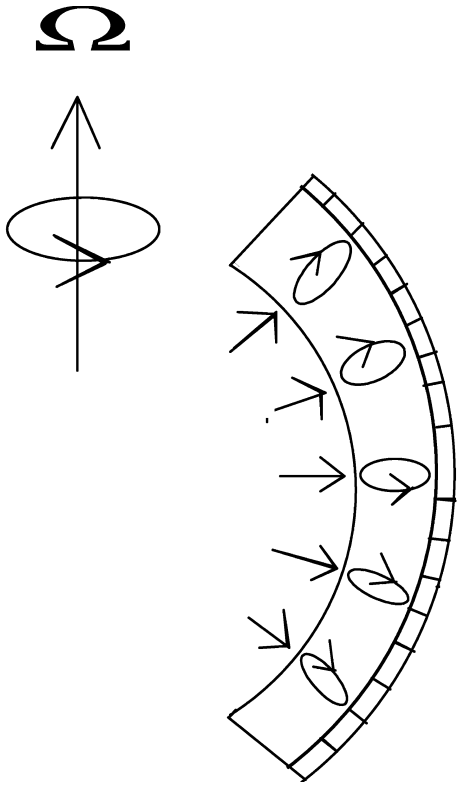

Figure 1. Longitudinal cross-section of the computational shell with rotation axis **Ω**. The input energy flux (straight arrows) is transported by convection (curly arrows) and then by radiation (shaded region), to the conducting top.

latitude, while the second, B, covers the same latitudinal range, but 60° in longitude. Both cover a total depth of $0.72R$ to R, which is the approximate depth occupied by the convection zone in the Sun. R is equivalent to the radius of the Sun. As depth is scaled by the total radius, the non-dimensional radius is between 0.72 and 1.0. Radial, meridional and zonal directions are labelled r (increasing outwards), θ (increasing southwards) and ϕ (increasing eastwards), respectively.

2.2 The equations

In the absence of motion ($\partial/\partial t = 0$, $\boldsymbol{v} = \boldsymbol{0}$), the equations governing conservation of mass, momentum and energy in a rotating stratified fluid (Chan 2001), reduce to the equations of hydrostatic and thermal equilibrium. A solution of these, in spherical coordinates, is a polytrope

$$T/T_{\rm t} = 1 + Z(R/r - 1)/(R/r_{\rm b} - 1), \tag{1}$$

$$\rho/\rho_{\rm t} = (T/T_{\rm t})^n, \tag{2}$$

$$p/p_{\rm t} = (T/T_{\rm t})^{n+1}, \tag{3}$$

where r is the radial distance from the base, and n is the polytropic index. The subscripts 't' and 'b' denote a quantity measured at the top and bottom of the shell, respectively. T, p and ρ are the symbols for temperature, pressure and density. $Z = (T_{\rm b} - T_{\rm t})/T_{\rm t}$ describes the extent of the stratification.

Equations (1)–(3) provide a reference atmosphere from which appropriate dimensionless units can be formed. Length is scaled by the outer radius of the shell R, and time by $R/\sqrt{p_{\rm t}/\rho_{\rm t}}$. In such units, velocity is scaled by the isothermal speed of sound at the top, $\sqrt{p_{\rm t}/\rho_{\rm t}}$. From now on all quantities will be given in non-dimensional units. Combining the equation of hydrostatic equilibrium, $\mathrm{d}p/\mathrm{d}r = -\rho g$ and equation (1), gives in non-dimensional units, $g_{\rm t} = (n+1)Zr_{\rm b}/(1 - r_b)$. We will consider $g_{\rm t}$ as an independent parameter. As the total number of pressure scaleheights is $(n+1)\ln(1+Z)$, the size of $g_{\rm t}$ determines the depth of the layer.

With such a scaling, the governing equations become

$$\partial\rho/\partial t = -\nabla\cdot\rho\boldsymbol{v}, \tag{4}$$

$$\partial\rho\boldsymbol{v}/\partial t = -\nabla\cdot\rho\boldsymbol{v}\boldsymbol{v} - \nabla p + \nabla\cdot\boldsymbol{\Sigma} - \rho g\hat{\boldsymbol{r}} - 2\rho\boldsymbol{\Omega}_0\times\boldsymbol{v}, \tag{5}$$

$$\begin{aligned}\partial E/\partial t = & -\nabla\cdot\left(\frac{1}{\gamma-1}\rho T\boldsymbol{v} + p\boldsymbol{v} + (\rho v^2/2)\boldsymbol{v}\right)\\ & -\nabla\cdot(-\boldsymbol{v}\cdot\boldsymbol{\Sigma} + \boldsymbol{f}) - \boldsymbol{\rho v}\cdot g\hat{\boldsymbol{r}},\end{aligned} \tag{6}$$

$$p = \rho T, \tag{7}$$

where $\boldsymbol{\Omega}_0$, $\boldsymbol{\Sigma}$ and $\boldsymbol{f}$ are defined below. Equations (4)–(7) represent a closed system of five dependent variables: density, radial mass flux, meridional mass flux, zonal mass flux and total energy density, denoted by ρ, ρv_r, ρv_θ, ρv_ϕ and E, respectively. In a particular geometry (fixed r, θ and ϕ boundaries), each turbulent convection simulation is specified by defining *six* non-dimensional parameters. These are the reference rotation rate Ω_0, the input energy flux at the base $f_{\rm b}$, the turbulent Prandtl number $\mathrm{Pr} = \nu/\kappa$, the gravitational acceleration at the top $g_{\rm t}$, the polytropic index n and the ratio of the specific heats γ.

We will now consider individual terms in equations (4)–(7). Ignoring the coefficient of bulk viscosity (Becker 1968), the viscous stress tensor for a Newtonian fluid is $\Sigma_{ij} = \mu(\partial v_i/\partial x_j + \partial v_j/\partial x_i) - 2\mu/3(\nabla\cdot\boldsymbol{v})\delta_{ij}$. In DNS, the viscosity is determined from the non-dimensional parameters characterizing the convection simulation (e.g. Pr, the Rayleigh number Ra, $g_{\rm t}$, n and γ). However, in LES, the dynamic viscosity μ is increased so that it represents the effects of Reynolds stresses on the unresolved or subgrid scales (SGS) (Smagorinsky 1963),

$$\mu = \rho(c_\mu\Delta)^2(2\boldsymbol{\sigma}:\boldsymbol{\sigma})^{1/2}. \tag{8}$$

The colon inside the brackets denotes tensor contraction of the rate of strain tensor $\sigma_{ij} = (\nabla_i v_j + \nabla_j v_i)/2$. The SGS eddy coefficient c_μ, is set to 0.2, the value for incompressible turbulence, and $\Delta^2 = r\Delta r\Delta\theta$ is an estimate of the local mesh size. Numerical experiments with different Δ and c_μ are described in Chan & Wolff (1982). The present formulation ensures that the grid Reynolds number $\Delta\times v/\nu$ is of the order of unity everywhere. To handle shocks, μ is multiplied by $1 + 2/c_{\rm s}^2[(\Delta x\partial_x v_x)^2 + (\Delta y\partial_y v_y)^2]$, where x and y denote meridional and zonal directions (e.g. $\Delta x = r\Delta\theta$ and $\Delta y = r\sin\theta\Delta\phi$) and $c_{\rm s}$ is the isothermal speed of sound. As μ is dependent on the horizontal divergence, any large horizontal velocity gradients are smoothed out by the increased viscosity.

The gravitational acceleration at a distance r from the centre of the sphere is $g\hat{\boldsymbol{r}}$, where $g = g_{\rm t}/r^2$, and $\hat{\boldsymbol{r}}$ is a unit vector directed radially outwards. The reference rotation vector is $\boldsymbol{\Omega_0} = \Omega_0\hat{\boldsymbol{\Omega}}$, where $\hat{\boldsymbol{\Omega}}$ is a unit vector in the direction of the rotation axis, i.e. $\hat{\boldsymbol{\Omega}}\cdot\hat{\boldsymbol{r}} = \cos\theta$. The non-dimensional rotation rate Ω_0, is equal to the ratio of the solar rotational velocity, to the isothermal speed of sound at the top of the convection zone. For the Sun Ω_0 is about 0.3, so that the value of 2.91 used in the present computation, is associated with rotational periods of about 1 day.

The total energy per unit volume E, is the sum of the internal energy $\rho T/(\gamma-1)$ and the kinetic energy $\rho v^2/2$. The terms in the brackets on the left-hand side of equation (6) are the various forms of energy flux in to or out of a unit volume fluid parcel. The first three terms constitute $(E+p)\boldsymbol{v}$, which equals the convective flux $c_p\rho T\boldsymbol{v}$ plus the kinetic energy flux $\rho v^2\boldsymbol{v}/2$. Away from the upper and lower boundaries $(E+p)\boldsymbol{v}$ represents the energy transported by the resolved large-scale eddies. The LES model is designed so that this term carries most of the vertical energy flux. The other fluxes from left to right, are the viscous flux and the diffusive flux, $\boldsymbol{f}$. The last term in the energy equation is the work done by buoyancy.

At the base $\boldsymbol{f}$ has a positive constant value. This is the source term of the vigorous turbulent convection, i.e. at $r = r_{\rm b} = 0.72$, $\boldsymbol{f} = f_{\rm b}\hat{\boldsymbol{r}}$. At all other horizontal levels $\boldsymbol{f}$ acts as a diffusion term, computed as $\boldsymbol{f} = -k_1\nabla S - k_2\nabla T$. The values of k_1 and k_2 determine whether the layer is convective (unstable) or radiative (stable). In the unstable layer ($0.72 \leqslant r < 0.986$), $k_1 = \mu T/\mathrm{Pr}$ and $k_2 \ll f_{\rm b}/|\nabla T|_{t=0}$. As k_2 is very small, nearly all of the heat transport is convective. In the upper layer ($0.986 \leqslant r \leqslant 1.0$), $k_1 = 0$ and $k_2 = f_{\rm b}/|\nabla T|_{t=0}$, allowing conduction to transport all of the heat flux in the stable layer. The conduction layer emulates radiation above the convection layer.

The horizontal boundaries are insulating, stress-free and impenetrable in latitude, and periodic in longitude. The top and bottom are both impenetrable and stress-free. The source term $f_{\rm b}$ is injected in at the bottom and conducted out through the top. This requires the top to be maintained at a constant temperature.

2.3 LES versus DNS

In the SCZ, as the convective flux $\gg$ diffusive flux, efficient

mixing reduces the superadiabatic gradient $\nabla - \nabla_{ad}$ to just above zero ($\approx 10^{-8}$). This type of convection is simulated numerically, by transferring energy from the base to the top of the computational domain as follows. First, in the unstable layer (from $r = 0.72$ up to $r = 0.986$) the gas conductivity is artificially small, forcing convection to carry most of the heat flux across the imposed temperature gradient. Secondly, the initial polytrope is neutrally stable $\left(\gamma = \frac{5}{3}, n = 1.5\right)$. After the convection has developed, the relaxed thermal structure remains very close to this initial state, so that ∇ is only slightly greater than ∇_{ad} (or equivalently ∇S is just below zero). This approach to modelling the SCZ is very different from the DNS approach. The main difference lies in the role of the diffusive flux. In the DNS by Brummel et al. (1996), radiation transports 75 per cent of the energy flux, while the resolved convective motions carry the rest (via the kinetic and enthalpy fluxes). In the present LES, the thermal conductivity is nearly zero, therefore even the entropy diffusion of the SGS, is greater than radiative diffusion. As $\nabla S \approx 0$, the resolved large eddies must carry the majority of the energy flux.

2.4 Angular momentum conservation

Owing to the non-zero reference rotation rate, after relaxation one must ensure that there is no mean motion between the fluid in the shell and the rotating frame of reference. After the start of the computation, the compressible bulk can acquire some spurious form of rotation caused by initial expansion or contraction. Enforcing the condition $\langle \rho v_\phi \rangle_v = 0$, where 'v' denotes volume averaging taken after thermal relaxation, ensures the total angular momentum is zero in the reference frame. This is accomplished by calculating the mean angular velocity of the shell, $\langle \Omega \rangle_v = \Sigma \rho v_\phi r \sin\theta / \Sigma \rho r^2 \sin^2\theta$, and subtracting the residual angular momentum from the total flow, $\rho v_\phi \rightarrow \rho v_\phi - \langle \Omega \rangle_v \rho r^2 \sin^2\theta$. When the statistics are gathered, $\langle \Omega \rangle_v$ is less than 4×10^{-4}.

2.5 Numerical methods

After some transformations to make the numerical scheme conservative and preserve second-order accuracy for the non-uniform vertical grid (Chan & Sofia 1986), equations (4)–(7) are discretized in spherical coordinates. Using a code developed by Chan & Wolff (1982), an implicit scheme (the alternating direction implicit method on a staggered grid or ADISM) relaxes the fluid to a self consistent thermal equilibrium. The relaxation time is of the order of a 'Kelvin Helmholtz' time ($\approx \int \rho c_v T \, dr / f_b$). In the fully relaxed layer, the energy flux leaving the top of the shell is within 5 per cent of the input flux f_b.

Next, a second-order explicit method (Adams–Bashforth time integration) gathers the statistics of the time-averaged state. The statistical integration time is over 500 turnover times, and requires about 1.5×10^6 time-steps. For model A (longitudinal span of 30°), there are $39 \times 70 \times 35$ grid points, in the radial, latitudinal and zonal directions, respectively. For model B, which has twice the longitudinal span of A, there are twice as many points in the longitudinal direction. The choice of grid comes from comparing a simulation in a very small section of the shell (Robinson 1999) ($\theta \pm 15°$), with a physically similar LES computation in a small box (Chan 2001). The box, which has an aspect ratio of 1.5, is placed at the mid-latitude of the shell.

For a single processor on the ORIGIN 2000, the CPU time per integration step is about 3 s in model B. Using automatic parallelization on four processors, the speed up factor is about 3. Numerical stability requires a non-uniform grid with the same number of grid points per scaleheight and a very small input flux f_b of 0.25/64. These significantly increase the total (implicit plus explicit) computation time. Consequently, the minimum time for a full simulation is about a month.

3 RESULTS

3.1 Trials

After a series of numerical experiments (Robinson 1999) in a shell spanning ±15° in latitude and longitude, a set of parameters were found that generated a 'Sun-like' rotation pattern. These were $\Omega_0 = 2.91$, $f_b = 0.25/64$, $\mathrm{Pr} = 1$ and $g_t = 19$ (about 5 pressure scaleheights). Fixing these parameters, the latitudinal span was increased to 60° (30° above and below the equator). Surprisingly, the rotation profile appeared to be in some kind of 'quasi-steady state'. Initially, a 'Sun-like' profile was seen, but as the computation progressed, the radial angular velocity gradient at the equator, switched from positive to negative. This simulation was run to completion and the averaged results are classified as model A.

Increasing Ω_0 did not improve matters, and only when the longitudinal span was increased to 60°, was a positive angular velocity gradient sustained. The shell now covered the same longitudinal as latitudinal extent. This simulation was run independently of model A and the averaged results are classified as model B. We found out later that the flow reversal in A, was caused by a spurious meridional circulation. Strong downflows at the impenetrable latitudinal boundaries generate a powerful flow, pointed from the equator towards the poles. This feature is described in Section 3.2.2.

3.2 Flow characteristics

In a turbulent fluid a quantity q can be split into a mean and a fluctuating part,

$$q = \bar{q}(r, \theta) + q'(r, \theta, \phi, t). \tag{9}$$

The overbar represents a combined longitudinal and temporal average, i.e.

$$\bar{q}(r, \theta) = \frac{1}{t_2 - t_1} \int_{t_1}^{t_2} \left(\frac{1}{(\phi_2 - \phi_1)} \int q \, d\phi \right) dt. \tag{10}$$

t_1 is the time after which the system has reached a self-consistent thermal equilibrium, i.e. $t_1 > \int e \, dr / f_b$. e is the internal energy at each horizontal level. The time required for statistical convergence $(t_2 - t_1)$ depends on the particular quantity being averaged. While the mean velocities required about 100 turnover times, turbulent quantities such as the velocity correlation $\overline{v_r' v_\phi'}$, took about 5 times as long.

3.2.1 Mean zonal flow

The angular velocity averaged over time and longitude, relative to the rotating frame of reference, is computed and shown in Figs 2 and 3 for model A, and in Figs 4 and 5 for model B. In model A, the isorotation contours are parallel to the rotation axis. This means the angular velocity of a fluid element at any point in the shell is determined by its perpendicular distance from the rotation

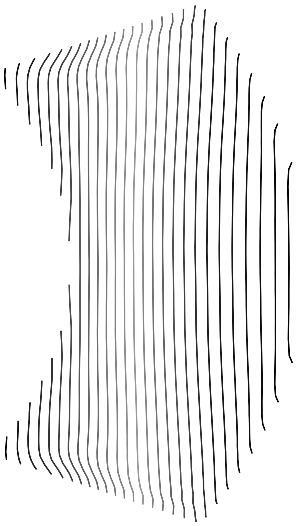

Figure 2. Isorotation contours averaged over time and longitude in a shell spanning 60° in latitude and 30° in longitude (model A).

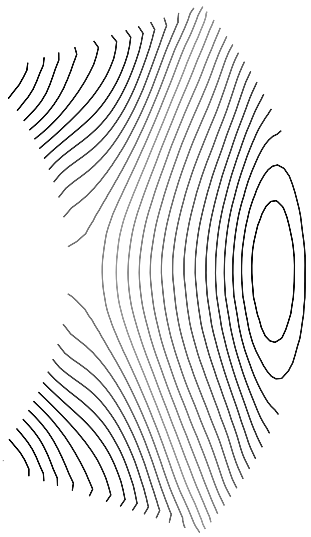

Figure 4. Isorotation contours averaged over time and longitude in a shell spanning 60° in latitude and longitude (model B).

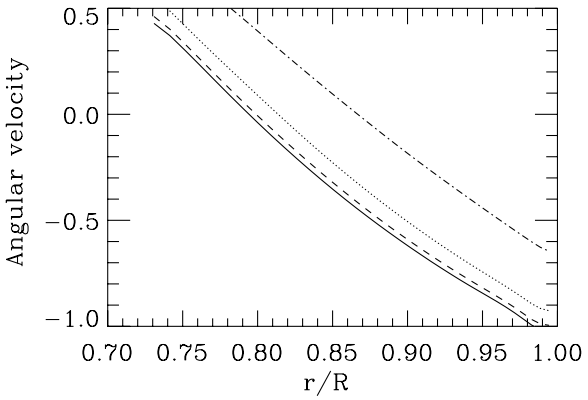

Figure 3. Depth variation of mean angular velocity in a shell spanning 60° in latitude and 30° in longitude (model A). Colatitudes of 90°, 85°, 79° and 67.5° are denoted by full, broken, dotted and chain curves, respectively.

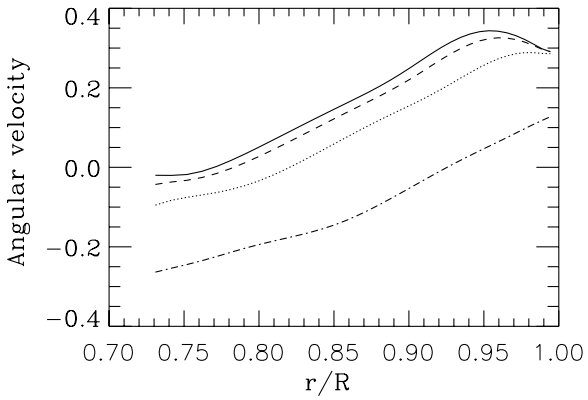

Figure 5. Depth variation of mean angular velocity in a shell spanning 60° in latitude and longitude (model B). Colatitudes of 90°, 85°, 79° and 67.5° are denoted by full, broken, dotted and chain curves, respectively.

axis. Fig. 3 shows the angular velocity plotted against non-dimensional depth (given as a fraction of the total solar radius, i.e. $r = r/R$) in the Northern hemisphere. Colatitudes (90°-latitude) of 90°,85°,79° and 67.5° are labelled by full, long-dashed, triple-dot-dashed and chain curves, respectively. The plots show that the angular velocity decreases radially outwards and away from the equator, in direct contrast with the rotational profile found in the SCZ.

If the simulation is repeated with twice the longitudinal span, the differential rotation has a much more 'Sun-like' appearance. In model B, the shape of the isorotation contours resemble helioseismology observations in two distinctive ways.

Firstly, an initial increase and then decrease in angular velocity from the top inwards near the equator is found, as shown by the two closed circular rotation contours (or equivalently, the radial angular velocity profile in Fig. 5). Helioseismic results, Kosovichev et al. (1997), show that the increase inwards of angular velocity occurs at the equator and up to 60° colatitude, but the behaviour at lower colatitudes is still unclear (Schou et al. 1999). As the computational shell only extends to about 60° colatitude, we will only consider behaviour away from the boundaries as being representative of the actual convective flow. In that sense, within ±8° about the equator, the computed angular velocity 'bump' is at least qualitatively similar to the observed result.

Secondly, away from the equator towards mid-latitudes, the contours are about half-way between the cylindrical contours (Taylor columns) seen in most earlier global simulations (e.g. Glatzmaier 1987), and the cone-like shape observed in the SCZ. There is also good agreement with recent anelastic global LES by Elliott, Miesch & Toomre (2000). Over the range of depth and latitude in common with their simulation and the present simulation, the isocontours are similar. The amount of variation of angular velocity with latitude is also in agreement with the SCZ. At the same colatitudes as in A, the mean angular velocity is plotted against depth (Fig. 5). At the top of the shell the angular velocity, drops by about 0.2 between the equator (full curve) and colatitude of 67.5° (chain curve). As Ω_0, is about 3, the drop implies a 7 per cent variation in rotation rate over 22.5°, or extrapolating, a pole that spins 28 per cent faster than the equator.

This is in rough agreement with the rotation rate at the surface of the Sun, which varies from 25 d at the equator to 35 d at the poles.

3.2.2 *Mean meridional flow*

The meridional flows are also very different. In A, a strong meridional circulation develops, directed from the equator towards the poles at the top, with strong downflows at the latitudinal boundaries. The mean meridional velocity $\overline{v_\theta}$ at the same colatitudes as used for the zonal flow, is presented in Fig. 6. As

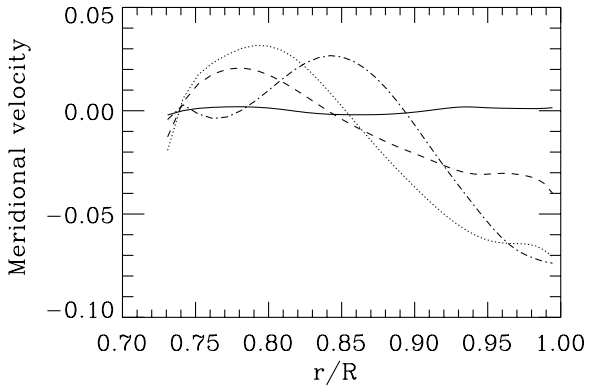

Figure 6. Depth variation of mean meridional velocity in a shell with a 30° longitudinal span (model A). Colatitudes of 90°, 85°, 79° and 67.5° are denoted by full, broken, dotted and chain curves, respectively.

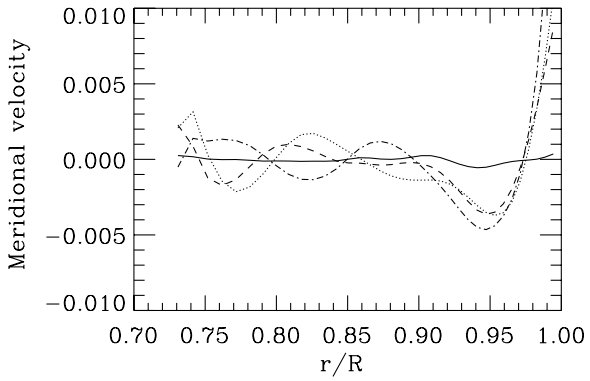

Figure 7. Depth variation of mean meridional velocity in a shell with a 60° longitudinal span (model B). Colatitudes of 90°, 85°, 79° and 67.5° are denoted by full, broken, dotted and chain curves, respectively.

$\overline{v_\theta} < 0$ in the Northern hemisphere, the upper leg of the circulation is directed from the equator to the pole. Moving polewards from the equator, where by symmetry the meridional velocity is zero, $|\overline{v_\theta}|$ increases to a maximum near a colatitude of 67.5°, and then reduces to zero as the flow approaches the latitudinal boundary. At the boundary, the magnitude of the maximum downward radial velocity (not shown) is about 0.2. The meridional circulation is produced by strong downflows associated with the stress free impenetrable boundaries. In early models of turbulent compressible convection in a small box, Chan & Sofia (1986), noticed that an impenetrable side boundary tends to attract downflows and they made all side boundaries periodic in later computations. In a shell that excludes the poles, impenetrable boundaries are unavoidable. These strong downflows create an artificially large meridional circulation.

Fortunately, the downflows can be almost eliminated by widening the longitudinal span. While the magnitude of the maximum radial velocity at the boundary is 0.2 in A, it is less than 0.005 in B (both being directed downwards). The impenetrable boundaries have very little effect on the downflows in B. This is because less restriction is placed on the flow direction. In A, the narrowness of the slice enhances the meridional circulation, enabling it to traverse the entire depth of the shell. In B, the meridional flow is only significant in the upper part of the shell ($r > 0.95$), elsewhere it is close to zero. Fig. 7 shows that $\overline{v_\theta}$ is negative (poleward) at the top of the unstable layer, while just above, in the stable layer, there is a returning (equatorward) flow. The return flow is twice as fast as the poleward flow, because the fluid at the top has half the density of the equatorward moving fluid, i.e. momentum is conserved in the meridional velocity loop. The point where $\overline{v_\theta}$ changes sign ($r = 0.975$) is very close to the beginning of the stable layer ($r = 0.985$). Below a depth of about 0.95, $\overline{v_\theta}$ is very small and the multicellular appearance is most probably a residual effect.

3.2.3 *Turbulent quantities*

The root-mean-square (rms) variance of a quantity q is given by

$$q'' = \sqrt{\overline{q^2} - \bar{q}^2}. \tag{11}$$

We can remove the radial dependence by averaging over the convection layer,

$$\langle q'' \rangle = \frac{1}{d} \int q'' \, \mathrm{d}r, \tag{12}$$

Table 1. Model A: turbulence characteristics in the 'non-Sun-like' differential rotation.

$\theta°$	$\langle\overline{v^2}\rangle^{1/2}$	$\langle v''\rangle$	$\langle v''_r\rangle$	$\langle v''_\theta\rangle$	$\langle v''_\phi\rangle$	Co	Re	Ta
67.5	0.361	0.094	0.064	0.059	0.035	8.6	330	2.1e+08
84	0.569	0.076	0.056	0.043	0.024	10.	290	2.5e+08
90	0.591	0.079	0.059	0.042	0.028	9.8	270	2.0e+08

Table 2. Model B: turbulence characteristics in the 'Sun-like' differential rotation.

$\theta°$	$\langle\overline{v^2}\rangle^{1/2}$	$\langle v''\rangle$	$\langle v''_r\rangle$	$\langle v''_\theta\rangle$	$\langle v''_\phi\rangle$	Co	Re	Ta
67.5	0.157	0.105	0.056	0.053	0.070	7.4	440	2.9e+08
84	0.238	0.122	0.065	0.063	0.080	6.3	480	2.6e+08
90	0.250	0.121	0.066	0.060	0.079	6.4	460	2.5e+08

where $d = 1 - r_b$ is the total depth of the layer. The angled brackets will be used to denote depth averages. Note $\langle q'' \rangle$ depends only on latitude.

Turbulent velocity characteristics at colatitudes of 90°, 84° and 67.5° are presented in Tables 1 and 2 for simulations A and B. The total kinetic energy (mean plus turbulent) is proportional to $\overline{\langle v^2 \rangle}^{1/2}$, while the turbulent part of the kinetic energy is measured by $\langle v'' \rangle$, where $v'' = \sqrt{v_r''^2 + v_\theta''^2 + v_\phi''^2}$. Columns 2 and 3 indicate the relative sizes of $\overline{\langle v^2 \rangle}^{1/2}$ and $\langle v'' \rangle$. In A, $\overline{\langle v^2 \rangle}^{1/2}$ is more than 4 times greater than $\langle v'' \rangle$, i.e. most of the kinetic energy is in the mean circulation. Conversely, in B, $\langle v'' \rangle$ is within a factor of 2 of $\overline{\langle v^2 \rangle}^{1/2}$, implying that the kinetic energy is split approximately equally between the mean and turbulent scales. In model B, most of $\langle v'' \rangle$ is in the zonal component $\langle v''_\phi \rangle$, while in A, $\langle v''_\phi \rangle$ is the smallest component. The distribution of kinetic energy between the mean and turbulent flow may determine the nature of the differential rotation. By measuring the autocorrelation function of the vertical velocity, we found that the vertical scale of the turbulence is about 1.5 pressure scaleheights (PSH), compared with a total shell depth of 5 PSH.

Non-dimensional parameters defining the importance of rotation compared with other physical processes can be calculated from the resultant flow. The strength of the turbulent convection relative to rotation is characterized by the Coriolis number, $\mathrm{Co} = \Omega_0 d / \langle v'' \rangle$. The Reynolds number, Re, compares the relative magnitudes of the advection and viscous terms, and is calculated as $\langle v'' \rangle d / \langle \bar{\mu}/\bar{\rho} \rangle$. The importance of SGS viscosity relative to rotation, is measured by the Taylor number, Ta, which is $4\Omega_0^2 d^4 / \langle \bar{\mu}/\bar{\rho} \rangle^2$ For reference these non-dimensional parameters are computed from the relaxed flow and presented in the last three columns of Tables 1 and 2. The Coriolis numbers are larger in A because the turbulent velocities are smaller. This suggests rotation will have a greater effect on the large scales in A than in B. The larger Reynolds numbers in B reflects the more turbulent nature of the flow.

4 DISCUSSION. WHAT PRODUCES THE DIFFERENTIAL ROTATION?

4.1 Taylor–Proudman balance (TPB)

Averaging the meridional momentum equation over longitude and time, so that $\partial/\partial\phi = 0$and $\partial/\partial t = 0$, produces

$$\frac{1}{r^2}\frac{\partial}{\partial r}(\overline{\rho v_\theta v_r} r^2) + \frac{1}{r\sin\theta}\frac{\partial}{\partial\theta}(\sin\theta\overline{\rho v_\theta^2}) + \frac{1}{r}(\overline{\rho v_\theta v_r} - \cot\theta\overline{\rho v_\phi^2}) + \frac{1}{r}\frac{\partial \bar{P}}{\partial\theta} - 2\Omega\overline{\rho v_\phi}\cos\theta + V_\theta = 0. \quad (13)$$

Measured at an arbitrary colatitude of 78°, Figs 8 and 9 show the relative sizes of terms in (13) computed from the averaged flows in A and B. From left to right terms are labelled by pluses, stars, diamonds, triangles, boxes and crosses, respectively. The third term in each equation is split into two terms (denoted by the diamonds and triangles). For the Co, Re and Ta values in the present simulations, the viscous stress terms V_θ are (equator excluded) much smaller than other terms. Therefore, these terms are not shown.

In both A and B the latitudinal pressure gradient (boxes) and the Coriolis force (crosses) are in approximate balance. The terms that contain the Reynolds stresses are insignificant. The overall dominance of the pressure gradient and the Coriolis force suggest the Navier–Stokes momentum equations can be approximated by

$$\frac{\nabla P}{\rho} = \boldsymbol{g} - 2\boldsymbol{\Omega}_0 \times \boldsymbol{v}. \quad (14)$$

The above equation is known as the Taylor–Proudman momentum balance. Using entropy $S = c_v \ln(p/\rho^\gamma)$ and the perfect gas equation $p = \rho \mathrm{R} T$, the curl of the left-hand side of (14) produces

$$\nabla \times \frac{\nabla P}{\rho} = -\frac{1}{\rho^2}(\nabla P \times \nabla \rho) = \nabla T \times \nabla S, \quad (15)$$

so that the ϕ component of the curl of equation (14) is equivalent to

$$2\Omega_0\left(r\cos\theta\frac{\partial v_\phi}{\partial r} - \sin\theta\frac{\partial v_\phi}{\partial\theta}\right) + \frac{\partial T}{\partial r}\frac{\partial S}{\partial\theta} - \frac{\partial T}{\partial\theta}\frac{\partial S}{\partial r} = 0. \quad (16)$$

As $\boldsymbol{g}$ can be written as a potential, the buoyancy term disappears.

Measurements from the simulation show that $\partial T/\partial r$ is nearly 3 orders of magnitude greater than $\partial T/\partial\theta$. The temperature field is almost radial and does not alter much from the initial unperturbed state. Assuming $T \approx T(r)$, the last term of (16) can be neglected,

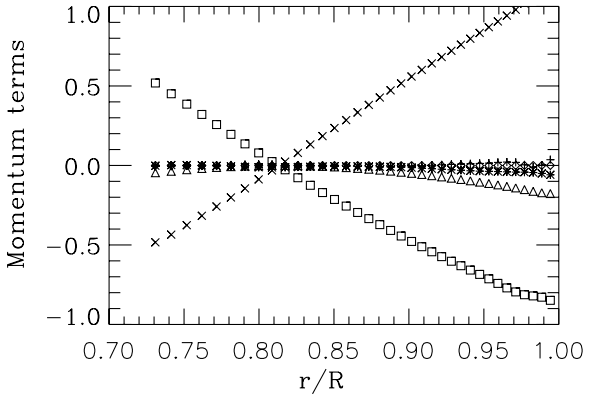

Figure 8. Successive terms in averaged meridional momentum equation measured at a colatitude of 78° in a shell with a 30° longitudinal span (model A). Clearly, the largest terms are the latitudinal pressure gradient (boxes) and the Coriolis force (crosses), while the Reynolds stresses are relatively insignificant.

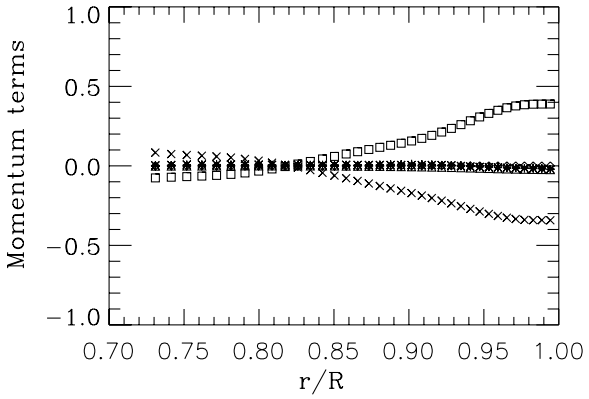

Figure 9. Successive terms in averaged meridional momentum equation measured at a colatitude of 78° in a shell with a 60° longitudinal span (model B). Similarly, the largest terms are the latitudinal pressure gradient (boxes) and the Coriolis force (crosses) and again the Reynolds stresses are very small.

and the second term can be replaced by

$$\frac{\mathrm{d}T}{\mathrm{d}r}\frac{\partial S}{\partial \theta} = -\frac{g(r)}{c_\mathrm{p}}\frac{\partial S}{\partial \theta} \tag{17}$$

which when substituted into (16), gives

$$2\Omega_0\left(r\cos\theta\frac{\partial v_\phi}{\partial r} - \sin\theta\frac{\partial v_\phi}{\partial \theta}\right) - \frac{g(r)}{c_\mathrm{p}}\frac{\partial S}{\partial \theta} = 0. \tag{18}$$

This is equivalent to the rotation law obtained by Durney (1999).

Fig. 10 shows the mean entropy, $\langle\bar{S}\rangle$ averaged over time, longitude and depth, plotted against colatitude for models A (triple-dot-dashed curve) and B (full curve). In A, the entropy is almost independent of colatitude, suggesting that $\partial S/\partial\theta \approx 0$, so that equation (18) reduces to

$$r\cos\theta\frac{\partial v_\phi}{\partial r} - \sin\theta\frac{\partial v_\phi}{\partial \theta} = 0. \tag{19}$$

Equation (19) implies $v_\phi = f(r\sin\theta)$, i.e. v_ϕ is constant along cylinders parallel to the rotation vector. In A because the pressure gradient and Coriolis terms dominate the momentum balance, and the latitudinal entropy gradient is approximately zero, Taylor columns are seen in the interior. This explains the isorotation contours in Fig. 3.

In contrast, in B the entropy varies significantly with colatitude. This non-zero latitudinal entropy gradient is the reason why more 'Sun-like' isorotation contours are seen in model B. In other words, the term $-g(r)/c_\mathrm{p}\cdot\partial S/\partial\theta$ shapes the differential rotation. Following this line of reasoning, we computed the baroclinic term $-g(r)/c_\mathrm{p}\cdot\overline{\partial S/\partial\theta}$ (denoted by boxes) and $2\Omega_\mathrm{o}(r\cos\theta\overline{\partial v_\phi/\partial r} - \sin\theta\overline{\partial v_\phi/\partial\theta})$ (denoted by crosses) from the averaged flow. Fig. 11 shows the results at colatitudes of 90° (smallest magnitude), 82° and 72° (largest magnitude). Clearly, they are in approximate balance, confirming that the *thermal structure, i.e. S(r, θ), directly controls the overall shape of the differential rotation profile. The Reynolds stresses play only a minor role in the dynamics*. As the simulation is of 'mildly', rather than fully developed turbulence, it remains to be seen, whether the same is true in the Sun.

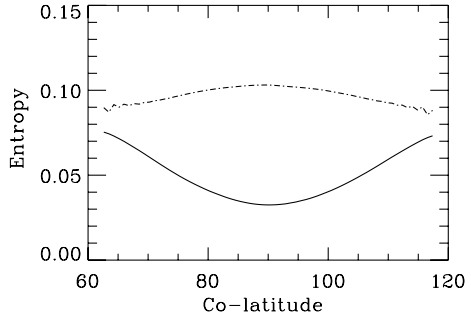

Figure 10. Longitude, time and depth averaged entropy variation with colatitude: simulations A and B are denoted by chain and full curves, respectively. The entropy is almost constant in model A, but has a significant latitudinal variation in B. In both cases the entropy gradient is zero at the equator.

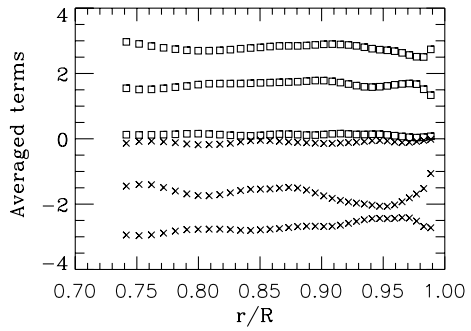

Figure 11. Averaged terms in the Taylor–Proudman balance for the shell with a 60° longitudinal span (model B). $-g(r)/c_\mathrm{p}\cdot\overline{\partial S/\partial\theta}$ and $2\Omega_\mathrm{o}(r\cos\theta\overline{\partial v_\phi/\partial r} - \sin\theta\overline{\partial v_\phi/\partial\theta})$, are denoted by boxes and crosses, respectively. Both expressions have the smallest magnitude at the equator and successively larger values at colatitudes of 82° and 72°.

4.2 Meridional circulation and the Reynolds stress

4.2.1 Meridional circulation produces differential rotation in A

In model A, meridional circulation drives the convection to a spurious equilibrium state (see sections 3.1 and 3.2.2). The computation starts off with a Sun-like rotational state, but as it progresses the layer relaxes to a completely different equilibrium. We previously suggested that this is a consequence of the artificially large downflows at the impenetrable latitudinal boundaries. We will now show that the direction and strength of the meridional circulation in A is just enough to drive the differential rotation.

Consider a fluid parcel in a Lagrangian frame of reference. Ignoring the zonal pressure gradient and frictional effects, the only force on the parcel is the Coriolis force associated with the meridional circulation (v_r,v_θ,0). The equation of motion of the fluid parcel is then

$$\mathrm{d}v_\phi/\mathrm{d}t \approx -2\Omega_0\cos\theta v_\theta - 2\Omega_0\sin\theta v_r. \tag{20}$$

Integrating with respect to time gives

$$\Delta v_\phi \approx -2\Omega_0\Delta(\sin\theta) - 2\Omega_0\sin\theta\Delta r. \tag{21}$$

We can verify this relation by taking values of $\overline{v_\phi}$ from Fig. 12 which shows how $\overline{v_\phi}$ varies with depth in model A. At the top of shell (constant r), $\Delta v_\phi/\Delta(\sin\theta) \approx 5.9$. While at the equator (constant θ), $\Delta v_\phi/\sin\theta\Delta r \approx -5$. As $\Omega_0 = 2.91$, the meridional circulation is about the right size and direction to produce the zonal velocity variation in A. This expresses as a tendency of fluid parcels to conserve their individual angular momentum.

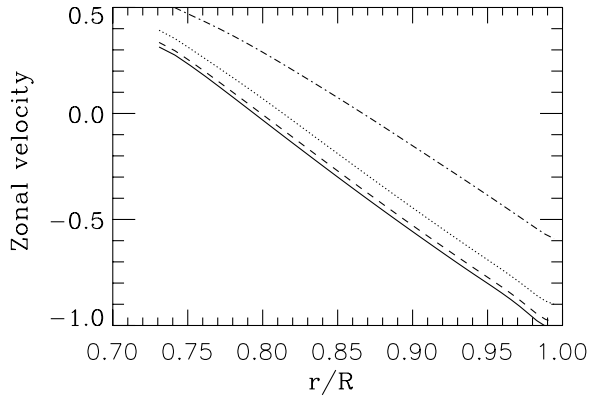

Figure 12. Longitude and time averaged zonal velocity in the narrower shell (model A). Colatitudes of 90°, 85°, 79° and 67.5° are denoted by full, broken, dotted and chain curves, respectively.

4.2.2 *Reynolds stress produces meridional circulation in B*

In model B, neither the meridional circulation, nor the Reynolds stress, are sufficient to directly drive the differential rotation. As previously described, it is the entropy distribution that produces the differential rotation in B. The meridional circulation in B is completely different to that in A. Equation (21) cannot be applied to the radial and latitudinal variation of zonal velocity in B. Fluid parcels do not appear to conserve their individual angular momentum. In fact, they do, it is just that other forces are involved, namely the Reynolds stresses.

In a turbulent fluid, the velocity can be split into its mean and fluctuating part. Though the average of the fluctuation is zero, the average of the product of two fluctuating quantities is not necessarily zero. The Reynolds stress is the averaged correlation between small-scale velocity fluctuations, in two component directions, and the density. To reduce the order of the statistical moments, we assume that density can be taken out of the correlation,

$$\overline{\rho v_i' v_j'} = \bar{\rho}\overline{v_i' v_j'}. \tag{22}$$

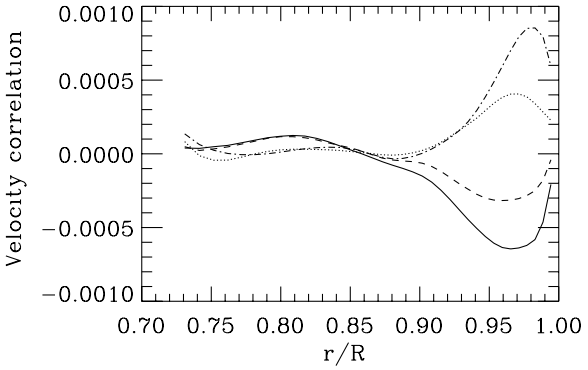

Figure 13. Longitude and time average of the product of radial and zonal velocity fluctuations $\overline{v_r' v_\phi'}$ (≈ Reynolds stress divided by mean density) versus depth (model B). Colatitudes of 90°, 85°, 79° and 67.5° are denoted by full, broken, triple-dot-dashed and chain curves, respectively. The negative troughs near the equator (full and broken lines) represents an inward transport of angular momentum by the Reynolds stress. The positive peaks away from the equator (dotted and dot-dashed lines) correspond to a change in the sign of the meridional velocity, indicating that $\overline{v_\theta}$ depends on the radial derivative $\overline{v_r' v_\phi'}$.

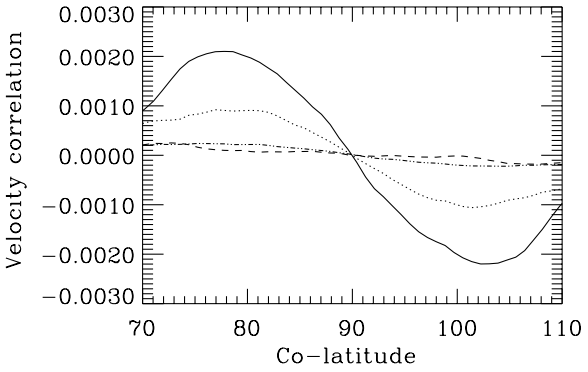

Figure 14. Longitude and time average of the product of meridional and zonal velocity fluctuations $\overline{v_\theta' v_\phi'}$ (≈Reynolds stress divided by mean density) versus colatitude (model B). Depths of 0.98, 0.95, 0.90 and 0.85 are denoted by full, dotted, broken and chain curves, respectively. Near the top (full and dotted curves) the latitudinal gradient of $\overline{v_\theta' v_\phi'}$ increases towards the equator.

This approximation is good because the density fluctuations are small (of the order of the square of the turbulence Mach number). This has been confirmed numerically. As the mean density only depends on depth, the nature of the Reynolds stress can be ascertained by looking at the velocity correlation, $\overline{v_i' v_j'}$. Fig. 13 shows $\overline{v_r' v_\phi'}$ plotted at the same colatitudes and using the same line markers as previous velocity plots. Fig. 14 shows $\overline{v_\theta' v_\phi'}$, at depths of 0.98, 0.95, 0.90 and 0.85, denoted by full, dotted, broken and chain curves, respectively.

By comparing the plots of $\overline{v_\theta}$ (Fig. 7) and the velocity correlations, certain features become apparent. First, quantities are only significant near the top of the shell (above $r = 0.90$), elsewhere they are close to zero. Secondly, at lower colatitudes (specifically 79° and 67.5°) the sign and order of magnitude of $\overline{v_\theta}$ closely matches negative the slope of $\overline{v_r' v_\phi'}$. Thirdly, towards the equator, $\partial/\partial r(\overline{v_r' v_\phi'})$ decreases, while $\partial/\partial\theta(\overline{v_\theta' v_\phi'})$ becomes steeper (more negative).

The relation between $\overline{v_\theta}$ and the Reynolds stresses (or velocity correlations), can be traced to the zonal momentum balance. In a rotating frame of reference, the axisymmetric zonal momentum equation can be written as

$$\frac{1}{r^2}\frac{\partial}{\partial r}(v_r v_\phi r^2) + \frac{1}{r\sin\theta}\frac{\partial}{\partial\theta}(v_\theta v_\phi \sin\theta) + N + 2\Omega_0(v_\theta\cos\theta + v_r\sin\theta) \approx 0, \tag{23}$$

where N denotes the additional non-linear terms and the viscous terms are again excluded. Near the impenetrable top boundary, v_r is close to zero, so the last term can be excluded. Clearly, the derivatives of $\overline{v_r' v_\phi'}$ and $\overline{v_\theta' v_\phi'}$ are capable of driving $\overline{v_\theta}$. Away from the equator $\overline{v_r' v_\phi'}$ drives $\overline{v_\theta}$, while close to the equator (specifically 85°) $\overline{v_\theta' v_\phi'}$ becomes more important.

Overall, the Reynolds stresses produce a weak meridional circulation concentrated in the uppermost part of the shell, but are negligible elsewhere.

4.2.3 *Reynolds stress produces an angular velocity 'bump' near the top*

One other feature of the zonal velocity profile that cannot be explained by the large-scale interaction of convection with rotation (i.e. TPB), is the small angular velocity 'bump' (see Fig. 5). The initial increase in angular velocity moving inwards can be considered as a small-scale feature of the flow ($\Delta\overline{v_\phi} <$ 1 per cent of the mean rotation rate). The 'bump' cannot be attributed to the large-scale entropy variation.

It seems likely that this small-scale feature could be caused by the Reynolds stress. The plot of $\overline{v_r' v_\phi'}$ (Fig. 13), reveals a connection between a negative drop in $\overline{v_r' v_\phi'}$ near the top of the shell, and the zonal velocity variation (Fig. 5). The negative trough near the equator at colatitudes of 90° and 85° (full and broken curves) represents an inward transport of angular momentum by the Reynolds stress. We suggest that this is the cause of the slight increase in angular velocity (or 'bump') moving inwards from the top of the convection zone. Furthermore, the maximum angular velocity at the equator, occurs at almost the same position as the minimum of $\overline{v_r' v_\phi'}$.

5 CONCLUSION

The aim of this work is to reproduce solar differential rotation, by solving the equations of hydrodynamics, in a section of a spherical

shell. To achieve this, we have performed two numerical simulations. The first simulation initially has an angular velocity that decreases inwards, in agreement with the solar case. However, as the computation progresses, the radial angular velocity gradient changes sign, and the rotation rate increases inwards. The mean rotational structure consists of cylindrical isorotation contours and a subrotating equator. The switch is caused by an artificially large meridional circulation, which itself is a result of strong downflows that occur at the impenetrable side boundaries.

In the second computation the longitudinal span is doubled, so that it now equals the latitudinal span. The wider shell has much weaker downflows and a more turbulent flow. Under these conditions the rotation profile remains in the 'Sun-like' state. The angular velocity now bears a closer resemblance to solar case, with a radial and latitudinal variation, both qualitatively and quantitatively similar to the SCZ.

By using an implicit time-stepping scheme, we are able to run the simulations for longer than a 'Kelvin Helmholtz' time-scale. The emphasis on complete thermal relaxation, could be the vital ingredient, required to correctly model rotating convection. Incomplete thermal relaxation, may be one reason why earlier simulations failed to obtain the proper rotation pattern. In the 'Sun-like' simulation, it is the *large*-scale thermal structure (specifically the entropy variation with latitude), rather than *small*-scale motions (as in mean-field models or some numerical models), that directly produces the differential rotation. The non-zero latitudinal entropy gradient (baroclinicity) shapes the differential rotation. We note that in the 'Sun-like' model, the kinetic energy distributes roughly equally between the mean and turbulent scales, in contrast to the non-'Sun-like' model, in which nearly all of the energy is in the mean flow. Furthermore, the turbulent kinetic energy is greatest in the zonal direction. This suggests the turbulent nature of the SCZ, may have some indirect role in the maintenance of solar differential rotation, but how it operates is still unclear.

The Reynolds stresses are important in the upper 10 per cent of the computational domain. This region contains the top of the convection (unstable) layer and all of the radiative (stable) layer. Here the velocity correlation $\overline{v_r' v_\phi'}$, has a dual effect. First, it provides an inward transport of angular momentum, which causes the slight increase in angular velocity, just below the surface and near the equator. Secondly, $-\partial/\partial r(\overline{v_r' v_\phi'})$ is principally responsible for the poleward meridional circulation at the top of the convection layer, and the accompanying return flow in the stable layer. Closer to the equator (within about 5°), $-\partial/\partial\theta(\overline{v_\theta' v_\phi'})$ appears to drive the meridional flow. In the meridional momentum equation (equator excluded) the only significant terms are the pressure gradient and the Coriolis force. The Reynolds stresses are only important in the zonal momentum equation, here they generate the meridional circulation found at the top of the shell.

The key result is that the dynamics near the top (surface layers) of the convection zone, are controlled by the Reynolds stresses, while elsewhere, the differential rotation is determined by the Taylor–Proudman momentum balance. A similar conclusion was reached in the semi-analytical model of the SCZ by Durney (2000) (and references therein).

ACKNOWLEDGMENTS

FJR would like to thank the Mathematics Department of the University of Newcastle Upon Tyne for their hospitality. The authors are grateful for comments from Bernard Durney, which led to significant improvements in this work. This paper was completed at the Astronomy Department of Yale University.

REFERENCES

Becker E., 1968, Gas Dynamics, Academic Press, New York, p. 229
Brummel N. H., Hurlbert N. E., Toomre J., 1996, ApJ, 473, 494
Chan K. L., 2001, ApJ, in press
Chan K. L., Sofia S., 1986, ApJ, 307, 222
Chan K. L., Wolff C. L., 1982, J. Comput. Phys., 47, 109
Durney B. R., 1999, ApJ, 511, 945
Durney B. R., 2000, ApJ, 528, 486
Elliott J. R., Miesch M. S., Toomre J., 2000, ApJ, 533, 546
Gilman P. A., 1978, Geophys. Astrophys. Fluid Dyn., 11, 157
Glatzmaier G. A., 1987, in Durney B. R., Sofia S., eds, The Internal Solar Angular Velocity. Reidel, Dordrecht, p. 263
Kosovichev A. G. et al., 1997, Sol. Phys., 170, 43
Libbrecht K. G., 1989, ApJ, 336, 1092
Miesch M. S., Elliott J. R., Toomre J., Clune T. L., Glatzmaier G. A., Gilman P. A., 2000, ApJ, 532, 593
Robinson F. J., 1999, PhD thesis, Hong Kong Univ. Science and Technology
Scherrer P. H. et al., 1995, Sol. Phys., 162, 129
Schou J. et al., 1999, ApJ, 505, 390
Smagorinsky J. S., 1963, Mon. Weather. Rev., 91, 99

This paper has been typeset from a TEX/LATEX file prepared by the author.